

Short Versus Long Range Exchange Interactions in Twisted Bilayer Graphene

Alejandro Jimeno-Pozo,* Zachary A. H. Goodwin, Pierre A. Pantaleón, Valerio Vitale, Lennart Klebl, Dante M. Kennes, Arash A. Mostofi, Johannes Lischner, and Francisco Guinea

This study discusses the effect of long-range interactions within the self-consistent Hartree-Fock (HF) approximation in comparison to short-range atomic Hubbard interactions on the band structure of twisted bilayer graphene (TBG) at charge neutrality for various twist angles. Starting from atomistic calculations, it determines the quasi-particle band structure of TBG with Hubbard interactions for three magnetic orderings: modulated anti-ferromagnetic (MAFM), (NAFM) and hexagonal anti-ferromagnetic (HAFM). Then, it develops an approach to incorporate these magnetic orderings along with the HF potential in the continuum approximation. Away from the magic angle, it observes a drastic effect of the magnetic order on the band structure of TBG compared to the influence of the HF potential. Near the magic angle, the HF potential plays a major role in the band structure, with HAFM and MAFM being secondary effects, but NAFM appears to still significantly distort the electronic structure at the magic angle. These findings suggest that the spin-valley degenerate broken symmetry state often found in HF calculations of charge neutral TBG near the magic angle should favor magnetic order, since the atomistic Hubbard interaction will break this symmetry in favor of spin polarization.

1. Introduction

Magic-angle TBG has generated tremendous interest in twistrionics^[1–3] since the discovery of correlated insulating states and superconductivity in the $\approx 1.1^\circ$ moiré superlattice.^[4,5] The initial reports^[4–6] indicated the presence of strong electron-electron correlations in TBG that give rise to unconventional superconductivity.^[5] While this is not unanimously agreed upon,^[7–11] TBG has also been found to host strange metal behavior,^[12,13] nematic order,^[14–17] Dirac revivals,^[18,19] Pomeranchuk effect,^[20,21] and Chern insulators,^[22–26] amongst other effects and phases.^[27–33]

To understand these phases, given that magic-angle TBG contains $\approx 12,000$ atoms in its moiré unit cell,^[34–37] it is typical for the low-energy continuum model,^[38,39] based on that of Bistritzer and MacDonald,^[40] to be utilized. This

A. Jimeno-Pozo, P. A. Pantaleón, F. Guinea
Imdea Nanoscience
Faraday 9, 28049 Madrid, Spain
E-mail: alejandro.jimeno@imdea.org

Z. A. H. Goodwin, V. Vitale, A. A. Mostofi, J. Lischner
Departments of Physics and Materials and the Thomas Young Centre for
Theory and Simulation of Materials
Imperial College London
South Kensington Campus, London SW7 2AZ, UK

Z. A. H. Goodwin
John A. Paulson School of Engineering and Applied Sciences
Harvard University
Cambridge, MA 02138, USA


V. Vitale
Dipartimento di Fisica
Università di Trieste
Strada Costiera 11, 34151 Trieste, Italy

L. Klebl
I. Institute of Theoretical Physics
University of Hamburg
Notkestrasse 9, 22607 Hamburg, Germany

D. M. Kennes
Institute for Theory of Statistical Physics
RWTH Aachen University, and JARA Fundamentals of Future Information
Technology
52062 Aachen, Germany

D. M. Kennes
Max Planck Institute for the Structure and Dynamics of Matter
Center for Free Electron Laser Science
22761 Hamburg, Germany

F. Guinea
Donostia International Physics Center
Paseo Manuel de Lardizabal 4
20018 San Sebastian, Spain

 The ORCID identification number(s) for the author(s) of this article can be found under <https://doi.org/10.1002/apxr.202300048>

© 2023 The Authors. Advanced Physics Research published by Wiley-VCH GmbH. This is an open access article under the terms of the Creative Commons Attribution License, which permits use, distribution and reproduction in any medium, provided the original work is properly cited.

DOI: 10.1002/apxr.202300048

theory couples states of the Dirac cones of each layer and valley at different moiré crystal momenta, which causes the onset of flat bands at $\approx 1.1^\circ$.^[8] The continuum model of TBG can naturally be extended to include long-ranged Hartree-Fock interactions,^[41] since it is based on an expansion in the moiré crystal momenta (which have very small magnitudes, corresponding to large length scales). This interacting theory has provided some understanding into the phase diagram of TBG,^[7,42] in terms of the superconducting phase,^[41,43–45] correlated insulating states,^[46–50] Dirac revivals,^[18] pinning of van Hove singularities,^[41,51] for example.

Including short-ranged interactions in this continuum model has proven more difficult, however. The Wannier orbital Hamiltonians of the flat bands,^[52–60] which provides a reduced Hamiltonian matrix that can be solved with strong-correlation methods,^[54,61–64] can include short-ranged interactions if computed (from an atomistic model), but there are also long-ranged interactions because of the extended nature of the Wannier orbitals, and therefore, the effect of short versus long ranged interactions cannot be decoupled. It is more natural to include short-ranged interactions in atomistic models, such as density functional theory (DFT)^[34,35] or tight-binding (TB),^[36,37] since the atomic-scale information is retained in such approaches. For example, Klebl and Honerkamp^[65] included an atomic on-site Hubbard interaction to study the magnetic phase diagram of TBG using random phase approximation (RPA) spin-susceptibility calculations.^[66,67] Moreover, these atomistic approaches can also include long-ranged interactions, such as self-consistent Hartree interactions.^[68–73]

A significant limiting factor of self-consistent atomistic approaches for broken symmetry phases is their computational cost.^[71,74,75] Some examples of such calculations exist in the literature,^[71–73,76] but modeling of the full phase diagram - as function of twist angle and doping level, amongst other experimental variables - has not yet been achieved. For example, González and Stauber^[72,73] used a Green's functions based method to study the effect of long-ranged interactions and the interplay between long and short-ranged interactions, but only at 1.16° and either at charge neutrality or -2 electrons per moiré unit cell. Moreover, Vahedi et al.^[71] investigated several twist angles (1.08° , 1.30° , and 1.47°), but only at charge neutrality. Often, the difficulty to access large system sizes has been mitigated by re-scaling the TB parameters^[71,77–79] or by applying hydrostatic pressure,^[80–82] such that flat bands can be studied using unit cells containing only a few hundred to a few thousand atoms.

Here, we develop an approach that includes short-ranged interactions, such as the on-site Hubbard interaction of the p_z orbitals, in the continuum model. Starting from the RPA spin susceptibility calculations of Klebl and Honerkamp,^[65] we perform self-consistent atomistic Hubbard calculations to obtain the mean-field magnetic order parameters for different ordering tendencies (at a large twist angle and charge neutrality). We develop analytical expressions for the real-space spin densities associated with the magnetic orderings. These analytical forms are then used to determine the corresponding scalar sublattice potentials to be used in continuum model calculations. In order to elucidate the twist angle dependence of the interplay between the magnetic orderings and the Hartree-Fock potential, we perform self-consistent Hartree-Fock calculations at charge neutrality, to

which we add the effective magnetic potential at different twist angles. Overall, it is found that the long-range contribution dominates at the magic-angle, but away from the magic angle, the effect of magnetic ordering is more significant. We discuss the competition between these long and short-range exchange interactions in detail, and finish with a discussion of future directions.

2. Results

2.1. Short- Range Atomistic Hubbard Interactions

From the RPA ($\mathbf{q} = 0$) spin-susceptibility calculations,^[65,66] three different leading magnetic orderings are identified: modulated antiferromagnetic order (MAFM), nodal antiferromagnetic order (NAFM) and hexagonal antiferromagnetic order (HAFM). To find which instability is the lowest energy state at a given twist angle and doping level, mean-field atomistic Hubbard calculations have been performed. As these atomistic calculations are extremely computationally expensive at the magic angle, we focus on 1.54° at charge neutrality, which is also motivation for $\mathbf{q} = 0$ magnetic instabilities, even though they might not be the true ground state. At this twist angle and doping level, RPA predicts the leading instability in TBG to be MAFM (with a critical Hubbard interaction of $U_c \approx 5.1$ eV), with NAFM and HAFM having slightly larger critical interaction strengths (of $U_c \approx 5.4$ eV). For these instabilities, we perform unconstrained and constrained atomistic Hubbard calculations, as outlined in Section Atomistic Calculations.

Figure 1b,c) show the spatial behavior of the MAFM instability obtained from mean-field Hubbard calculations with $U = 5.4$ eV. The magnetic order parameter is characterized by a sub-lattice oscillation of the magnetic order parameter $\zeta = (n_l - n_r)/(n_l + n_r)$, which is modulated throughout the moiré supercell.^[65] Figure 1b displays the magnetic structure along the diagonal of the moiré unit cell of the top graphene layer, with sublattice A and B plotted separately in black and gray, respectively. Figure 1c additionally illustrates the real-space structure of the magnetic order parameter on sublattice B of the top layer over the moiré supercell. The moiré-scale variation of the MAFM order is not large enough to change the sign of the sublattice polarization. The magnetic order parameter exhibits a peak in the AA region, as might be expected from the LDOS of TBG.^[36] At the peaks, we find that the magnetic order parameter has a value of $|\zeta| \approx 0.1$ suggesting that not just the flat-band electrons are spin polarized (otherwise, one could expect a value of $|\zeta| \approx 10^{-4}$). This is in agreement with other works.^[71–73]

The MAFM order can be approximated with the following analytical form

$$\zeta^M(\mathbf{r}) \approx \zeta'_s + \frac{\zeta_s}{6} \sum_{i=1}^6 \cos(\mathbf{G}_i \cdot \mathbf{r}) \quad (1)$$

where \mathbf{G}_i are reciprocal lattice vectors, ζ'_s is the average sublattice polarization and ζ_s describes how this sublattice polarization changes on the moiré scale. For sublattice A_l (B_l), where $l = 1, 2$ is the layer index, the sign of the polarization is $-$ ($+$). Note that the above equation assumes the AA region is located at the origin of the moiré unit cell.

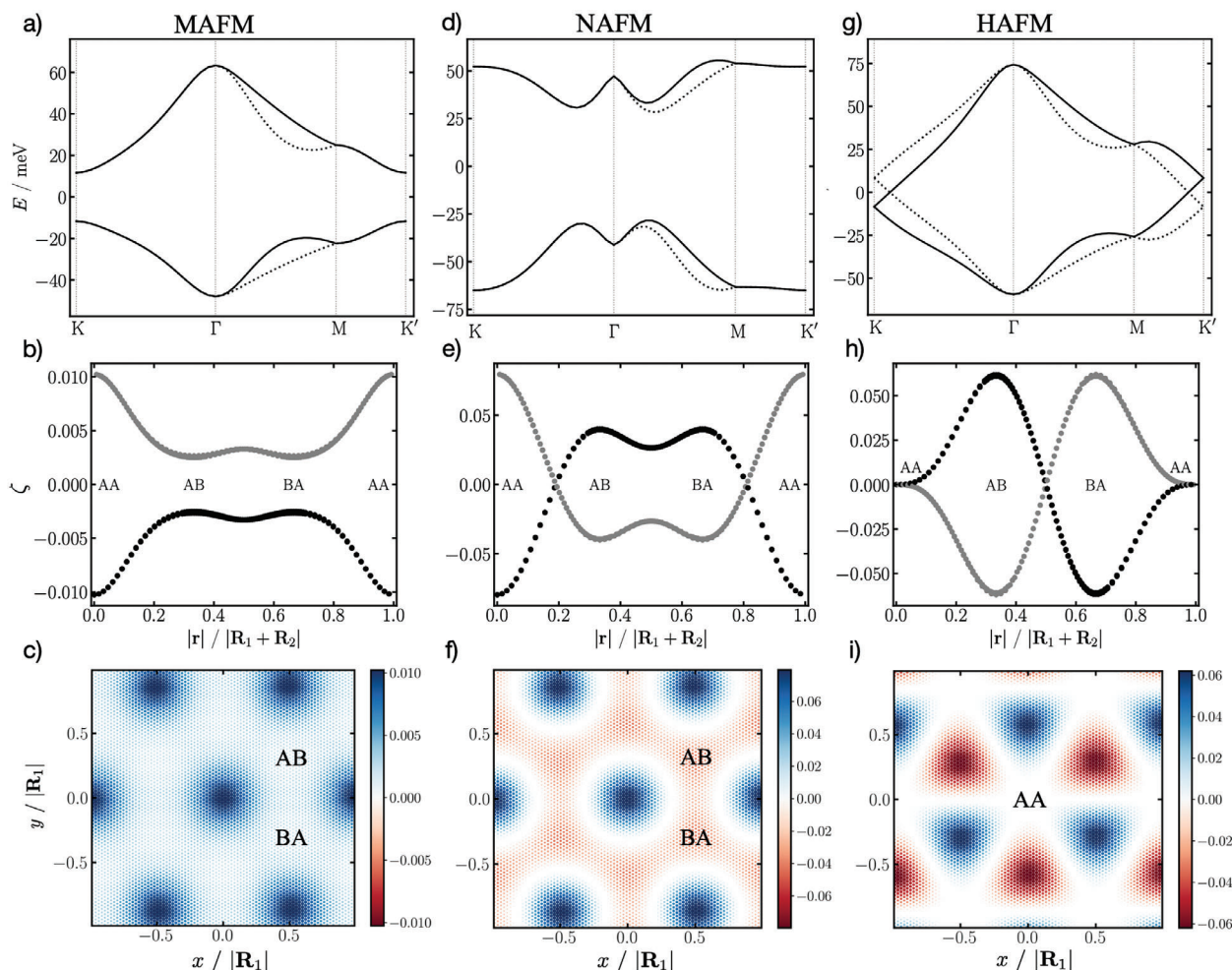


Figure 1. a,d,g) Self-consistent quasi-particle band structures for the studied magnetic orders of TBG at 1.54° and charge neutrality along the high symmetry path. For MAFM, $U = 5.4$ eV and unconstrained calculations were performed; whereas, for NAFM and HAFM, $U = 5.94$ eV and constrained calculations were performed. b,e,h) Corresponding self-consistent magnetic order parameter plotted along the diagonal of the moiré superlattice, where \mathbf{R}_1 and \mathbf{R}_2 are the moiré lattice vectors. Sublattice A is shown in black and sublattice B is shown in grey for the top graphene layer (bottom layer not shown). c,f,i) Corresponding plots in real space for a single layer and sublattice, where only sublattice B of the top layer is shown. Note, the U 's were chosen to be slightly above the critical values. For MAFM, if $U = 5.94$ eV is used, the gap at the Dirac point is extremely large.^[83]

In Figure 1a, we show the corresponding self-consistent quasi-particle band structure. The different valleys, K and K', have been identified by applying the valley operator to the states (see Refs. [78, 79, 84] for details of this calculation), and shown in solid black and dotted grey, respectively. Since the MAFM order breaks C_2 symmetry, it causes a gap to open at the Dirac cones at the K/K' points of the moiré Brillouin zone of TBG.

Finally, we point out that the MAFM order could not be stabilized at $U = 5.1$ eV, but it was found to be stable for all larger values of U . For U larger than 5.4 eV, the constant contribution dominates, i.e., $\zeta'_s \gg \zeta_s$, with the gap at the K/K' points becoming very large (100's of meV).^[83]

Similarly, the order parameter in the NAFM order also exhibits a peak in the AA regions. In contrast to MAFM, the average of the sublattice spin polarization over the moiré unit vanishes, as seen in the self-consistent values shown in Figure 1e. The corresponding real-space structure is shown in Figure 1f, where nodes in the magnetic order around the AA region separate the regions of op-

posite signs of spin polarization. This magnetic order is referred to as nodal anti-ferromagnetic order because ζ goes through zero between the AA and AB/BA regions, causing the sign of ζ to change on each sub-lattice between these types of stacking.^[65] It can be described by

$$\zeta^N(\mathbf{r}) \approx \frac{\zeta'_s}{6} \sum_{i=1}^6 \cos(\mathbf{G}_i \cdot \mathbf{r}) \quad (2)$$

This instability was not the leading instability,^[65] and we found the unconstrained calculations could never stabilise this order, as it would always eventually revert to MAFM order. Therefore, we performed constrained mean-field Hubbard calculations, as explained in Section Atomistic Calculations. The resulting quasi-particle band structure for $U = 5.94$ eV is shown in Figure 1d, and again it is an antiferromagnetic, Mott-like insulator with a large gap. Using the constraint method, the NAFM order could be stabilized for U values larger than 5.67 eV.

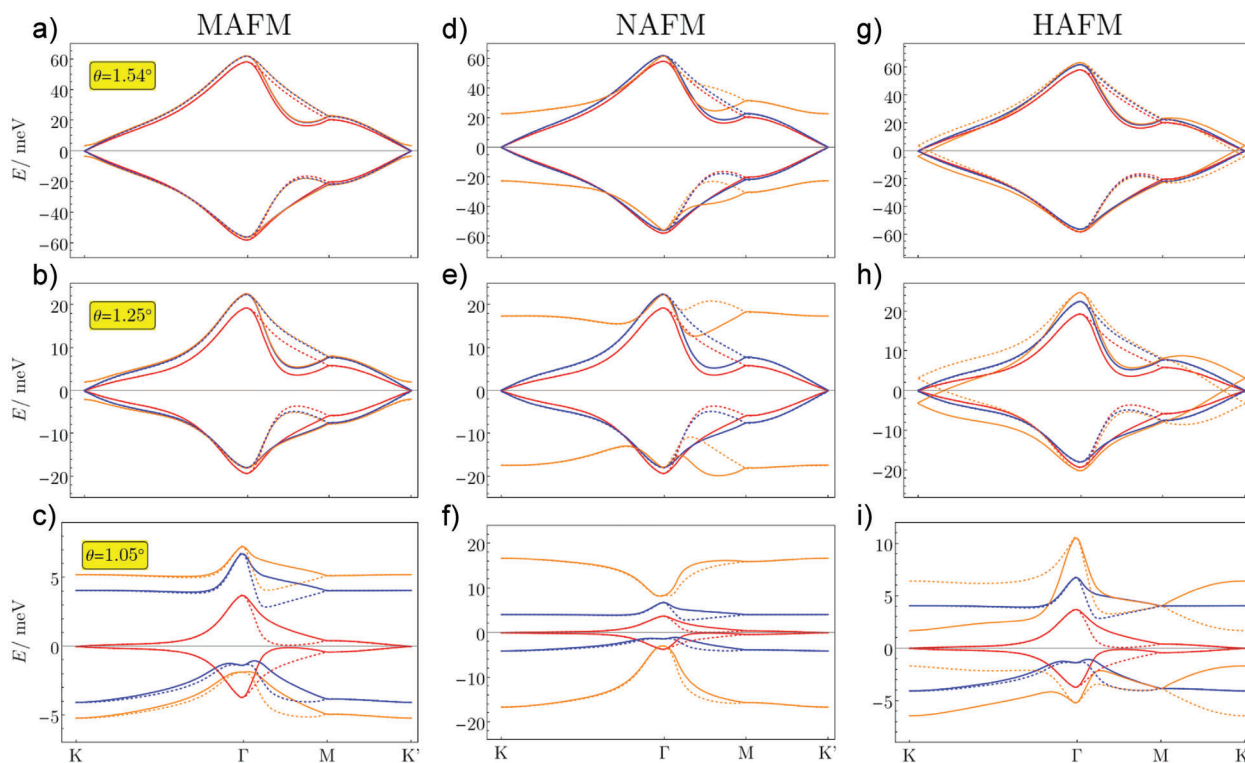


Figure 2. Comparison of low energy band structure, along the path $K \rightarrow \Gamma \rightarrow M \rightarrow K'$ in the mBZ, of the non-interacting case in red, HF in blue and HF+MAFM (a, b, c), HF+NAFM (d, e, f), HF+HAFM (g, h, i) in orange, for $\theta = 1.54^\circ$ (a, d, g), $\theta = 1.25^\circ$ (b, e, f) and $\theta = 1.05^\circ$ (c, f, i). Dashed lines correspond to valley flip.

Finally, the HAFM instability is similar to NAFM, but the magnetic order parameter peaks on the AB/BA regions instead of the AA regions. The self-consistent HAFM magnetic structure is shown in Figure 1h and i). The sign of ζ changes between the AB and BA regions of the moiré unit cell. As the peaks of ζ occur on the AB/BA regions, which form a hexagonal lattice on the moiré scale, this ordering is referred to as hexagonal anti-ferromagnetic order. This magnetic order is shown in Figure 1h,i, and can be described by the analytical form

$$\zeta^H(\mathbf{r}) \approx \frac{\zeta_s}{6} \sum_{i=1}^6 \sin(\mathbf{G}_i \cdot \mathbf{r}) \quad (3)$$

This instability never appears as a leading instability, but its critical Hubbard interaction was found to be ≈ 5.4 eV, which is only slightly higher than the leading MAFM instability. We again found that constrained calculations were required to obtain mean-field values of its order parameter, as explained in Section Atomistic Calculations. In Figure 1g, we show the mean-field quasi-particle band structure for $U = 5.94$ eV (this was the smallest U which could stabilize the order with constrained calculations), where the different valleys have been colored solid black and dotted grey. We find that this magnetic order does not create a gap at the K/K' point, despite exhibiting a sublattice oscillation. This is because it does not break C_2 on the moiré scale. It does cause the valleys to split at the K/K' points, however, resulting in one valley being pushed higher in energy and the other to lower energies. This is similar to the effect of a perpendicular electric field.

In summary, the atomistic calculations give detailed insights into the magnetic order induced by Hubbard interactions in TBG. However, it is not possible to carry out such calculations close to the magic angle and we had to use values of U that are significantly larger than the physical value of ≈ 4.5 eV^[77,85,86]. To overcome the limitations of the atomistic approach, we now aim to incorporate the effects of atomic Hubbard interactions into the continuum model of TBG.

2.2. Long-Range Interactions in the Continuum Model

In Figure 2, we show the Hartree-Fock quasi-particle band structure (solid blue line, for all subplots) for a number of twist angles at charge neutrality, in addition to the non-interacting band structure (solid red line, for all subplots). At 1.54° , Figures 2a,d,g, we find that the Hartree-Fock potential slightly modifies the non-interacting band structure, indicating that this twist angle is too large for the formation of an insulating state. At a twist angle of 1.25° , Figures 2b,e,h, the non-interacting bands are flat enough for the onset of a small gap due to the Hartree-Fock potential, significantly smaller than the bandwidth, at the Dirac cones K and K' points in the moiré Brillouin zone. Right at the magic angle of 1.05° , Figures 2c,f,i, the Hartree-Fock interactions induce a large gap at the K and K' points, on a similar scale to the bandwidth. At charge neutrality these insulating states are characterized by a broken sublattice symmetry and a preserved spin and valley symmetry with respect to the non-interacting picture. This implies that the mean-field ground state associated with the

Table 1. Parameters $|\delta_1|$ and $|\delta_2|$ extracted from the atomistic Hubbard calculations for the different orderings considered in this work. All values are expressed in meV.

Order	$ \delta_1 $	$ \delta_2 $
MAFM ($U = 5.4$ eV)	12.47	12.54
NAFM ($U = 5.94$ eV)	0	237.09
HAFM ($U = 5.94$ eV)	0	211.89

Hartree-Fock band structure is a linear combination of four states with different spin and valley indices. These calculations are in good agreement with a large body of literature, which investigates these long-ranged interactions.^[7,8,42]

2.3. Short-Range Interactions in the Continuum Model

Given the form of the anti-ferromagnetic orders discussed in Section 2.1, we include them within the continuum model by means of a scalar potential expanded in the first star of the BZ, as discussed in the Experimental Section. For the MAFM instability both δ_1 and δ_2 are real valued. In the case of NAFM, since the sublattice spin polarization averages to zero $\delta_1 = 0$, and δ_2 is a real number. Similarly for the HAFM instability $\delta_1 = 0$, but δ_2 is a purely imaginary number so the modulation is a sine function. Both MAFM and NAFM orderings are degenerate in the valley index but the HAFM is not and the modulated contribution to the potential must be complex conjugated when exchanging valleys. The value of the parameters δ_1 and δ_2 are obtained numerically within the self-consistent atomistic Hubbard calculation at a twist angle of 1.54° and at charge neutrality, as described in Section 2.1. Their values for the different magnetic orders are summarized in Table 1. In the Appendix, we show the band structures in the continuum model (without the Hartree-Fock contribution) at 1.54° when the magnetic potential is included and find good agreement with the atomistic calculations.

Next, we combine the Hubbard potential with the long-ranged Hartree-Fock potential to study the band structure of TBG near the magic angle. The values of δ_1 and δ_2 at smaller twist angles can be obtained from $|\delta_{1/2}(\theta)| = |\delta_{1/2}(1.54^\circ)| \left(\frac{\theta}{1.54^\circ}\right)^2$.^[41] However, as discussed above, the atomistic Hubbard calculations were carried out for U values that are larger than the physical U . As a result, the band gap obtained near the magic angle are much larger than experimental findings, see Figure A2. To obtain physically reasonable results, we reduce δ_1 and δ_2 by an additional scaling factor, see discussion in the Appendix.

In Figure 2 we show band structures with a scaling factor of 1/3. Results for other scaling factors are shown in the Appendix. Note that electron densities obtained from Hartree-Fock theory can also exhibit sublattice polarization. When this happens, the sublattice-polarized magnetic potential can be added in two inequivalent ways. In our calculations, we always choose relative the sign such that the sublattice polarization matches in the Hartree-Fock result and the Hubbard result, as this should increase any bandgaps and reduces the total energy.

First, we discuss the Hartree-Fock result with the MAFM order, as shown in Figures 2a–c. At a twist angle of 1.54° , Figure 2a, we find that the magnetic order induces a small gap at the K/K'

points, which is absent in the pure Hartree-Fock result. For a smaller twist angle of 1.25° , Figure 2b, a similar situation is found: the magnetic order opens a gap at the K/K' points while the Hartree-Fock potential is responsible for minor changes in the band structure compared to the non-interacting result. At the magic angle of 1.05° , Figure 2c, the situation changes dramatically: now the magnetic potential only slightly modifies the gap at the K/K' points, while the Hartree-Fock contribution dominates the deformations to the electronic structure.

Next, we move on to describing the results for NAFM ordering, as seen in Figure 2d–f. At the largest twist angle of 1.54° , Figure 2d, this magnetic order creates a significant gap at the K/K' points. This large magnitude of the gap could be an artifact of the non-self-consistent nature of the calculations or result from an overestimate of the parameters that determine the magnetic potential. These large band deformations persist at the smaller twist angles of 1.25° , Figure 2e, and 1.05° , Figure 2f. Even if smaller values of the parameters are utilized (by using a scaling factor that is smaller than 1/3), this NAFM order induces large band deformations, lowering the energy of the occupied valence band. Therefore, it appears that this magnetic order can compete with the Hartree-Fock contribution even at the magic angle.

Finally, we describe the effect of HAFM. As can be seen in Figures 2g–i, the HAFM order does not create a gap at the K/K' points. Instead it causes the Dirac cones at K and K' to shift up and down, respectively, for the single spin and valley channel. At 1.54° , Figure 2g, this effect is almost imperceptible but stronger than the one induced by the Hartree-Fock interactions. For the smaller twist angle of 1.25° , Figure 2h the situation is similar but the energy gap between K and K' increases. While at the magic angle, Figure 2i, it slightly contributes to reshaping the band structure, which in contrast is heavily affected by the Hartree-Fock contribution, so we can safely say that the HAFM is a secondary effect in this case.

3. Discussion

Overall, it appears that the MAFM, NAFM, and HAFM magnetic potentials are more significant away from the magic angle, but at angles close enough that there could still be broken symmetry phases.^[26,66] For example, 1.25° seems to be the most significantly affected by these Hubbard potentials relative to the exchange contribution. At the magic angle, the exchange contribution dominates, and at large twist angles the effects are small relative to the bandwidth, suggesting that the MAFM, NAFM, and HAFM magnetic orders are not significant at these twist angles. This twist angle dependence could suggest why the predictions of Klebl et al.,^[66] in terms of the twist angle and doping dependence of magnetic states, agreed well with subsequent experiments.^[26] This could be because these Hubbard interactions are important close to the onset of broken symmetry phases, but close to the magic angle these Hubbard interactions are dominated by long-ranged Hartree-Fock interactions.^[41]

The NAFM order appears to affect the electronic structure most significantly, both at the magic angle and away from it, causing the occupied eigenvalues of the valence band to decrease, and therefore, it is a possible candidate for magnetic order in TBG. In contrast, the MAFM order affects the electronic structure more weakly. Finally, the HAFM appears to only affect the electronic

structure slightly. This magnetic order should, however, couple to perpendicular electric fields,^[77,83] which could make this ordering tendency more important. These perturbative calculations are interesting because they are a very natural explanation for the correlated insulating states in TBG.^[4] From the Hartree-Fock calculations, a spin-valley degenerate insulating state is obtained. The atomistic Hubbard interaction, however, should break this symmetry and cause the onset of magnetic order.

We have focused on TBG here, but many more moiré materials comprised of graphene exist.^[87,88] Perhaps the most promising ones are where there is a $\pm\theta$ twist between each adjacent graphene layer.^[84,89–95] These moiré graphene multilayers have been shown to host highly tunable superconducting phases,^[96–100] and as the number of layers increases, the superconducting phase occurs over wider and wider doping ranges.^[101,102] Fischer et al.^[93] has shown similar types of magnetic order occur in these systems, which means it will be possible to use the developed method. Another example of moiré structures is graphene twisted on a graphene multilayer, such as twisted mono-bilayer graphene.^[103,104] The magnetic structure of these systems was shown to be more complex by Goodwin et al.,^[105] which suggests the approach described here could be difficult to utilize. Finally, another class of moiré graphene multilayers is twisted bilayers composed of graphene multilayers, such as twisted double bilayer graphene.^[106–111] Further investigation of this system would be of interest.

Apart from moiré graphene multilayers, moiré-less graphene heterostructures have recently shown superconductivity and strongly correlated phases^[112–114] and therefore have drawn great attention.^[115] Due to the small Fermi surfaces, theoretical models often only treat the long-ranged part of the Coulomb repulsion.^[116–120] Our work demonstrates that in principle both long- and short-ranged interactions can have a significant effect on spin and valley order and therefore encourages further research in this direction for non-moiré graphene heterostructures.

Moreover, one main assumption of the presented calculations is that the magnetic instability is $\mathbf{q} = 0$ with collinear spins. While these are simple approximations, which permitted us to develop a method for translating the instabilities from atomistic models to continuum models, the MAFM, NAFM, and HAFM magnetic instabilities are not necessarily the ground state, as shown in Ref. [71], for example. Therefore, a future direction of research would be to further develop the method to include $\mathbf{q} \neq 0$ and non-collinear spins.

4. Conclusion

In summary, starting from atomistic methods, we studied several leading magnetic instabilities of charge neutral TBG at a large twist. From these numerical calculations, we extracted analytical expressions for the potentials of different magnetic orderings, which allowed us to effectively include them within the continuum model. The Hubbard calculations have been performed self-consistently using atomistic methods, while the Hartree-Fock approximation has been computed self-consistently using the continuum model. When, we introduce the magnetic orderings as effective potentials in the continuum model, we do not seek further self-consistency, instead we add them as a perturbation to the Hartree-Fock Hamiltonian, allowing a comparison of long-

and short-range exchange interactions. From these calculations, we draw the following conclusions:

1. Atomistic Hubbard interactions break the spin-valley degeneracy of the insulating state at charge neutrality of TBG obtained from self-consistent Hubbard calculations. Therefore, these calculations suggest a Mott-like insulating state.
2. The effect of the magnetic orders is most significant for intermediate twist angles between the magic-angle and angles where non-interacting physics is sufficient. At the magic angle, the Hartree-Fock contribution dominates, and at large angles the bandwidth dominates.
3. Out of the studied magnetic orders, nodal anti-ferromagnetic order appears to be the most significant for changes to the electronic structure, both at and away from the magic angle.

It is hoped that these results will further motivate the inclusion of atomistic effects in the continuum model. Moreover, performing self-consistent magnetic calculations should also be possible, and investigating such ordering tendencies in other moiré graphene multilayers is now possible.

5. Experimental Section

Atomistic Calculations: This study commensurate moiré unit cells of TBG,^[36] starting from AA stacked bilayers and rotating the top layer anti-clockwise about an axis perpendicular to the graphene sheets that passes through a carbon atom in each layer. The moiré lattice vectors of the commensurate structures were $\mathbf{R}_1 = n\mathbf{a}_1 + m\mathbf{a}_2$ and $\mathbf{R}_2 = -m\mathbf{a}_1 + (n+m)\mathbf{a}_2$, where n and m are integers that define the commensurate TBG structure, and $\mathbf{a}_1 = (\sqrt{3}/2, -1/2)a_0$ and $\mathbf{a}_2 = (\sqrt{3}/2, 1/2)a_0$ are the lattice vectors of graphene, where $a_0 = 2.46 \text{ \AA}$ is the lattice constant of graphene.

At small twist angles, TBG undergoes significant atomic relaxations.^[34,35,121–125] It calculate these relaxations using a classical force field implemented in the LAMMPS software package.^[126] The interlayer interactions were modeled using the AIREBO-Morse potential,^[127] while intralayer interactions are described with the Kolmogorov-Crespi (KC) potential.^[128]

To investigate the electronic structure of TBG, the Hamiltonian was used

$$\hat{H} = \sum_{i\sigma} \epsilon_{i\sigma} \hat{c}_{i\sigma}^\dagger \hat{c}_{i\sigma} + \sum_{j\sigma} [t(\mathbf{r}_i - \mathbf{r}_j) \hat{c}_{j\sigma}^\dagger \hat{c}_{i\sigma} + \text{H.c.}] \quad (4)$$

where $\epsilon_{i\sigma}$ and $\hat{c}_{i\sigma}^\dagger$ ($\hat{c}_{i\sigma}$) denote the on-site energy of atom i with spin σ and the electron creation (annihilation) operator associated with atom i and spin σ , respectively. The hopping parameters between atoms i and j , $t(\mathbf{r}_i - \mathbf{r}_j)$, were calculated using the Slater-Koster (SK) rules^[129]

$$t(\mathbf{r}) = V_{pp\sigma}(\mathbf{r}) \left(\frac{\mathbf{r} \cdot \mathbf{e}_z}{|\mathbf{r}|} \right)^2 + V_{pp\pi}(\mathbf{r}) \left(1 - \frac{\mathbf{r} \cdot \mathbf{e}_z}{|\mathbf{r}|} \right)^2 \quad (5)$$

where $V_{pp\sigma}(\mathbf{r}) = V_{pp\sigma}^0 \exp\{q_\sigma(1 - |\mathbf{r}|/d_{AB})\} \Theta(R_c - |\mathbf{r}|)$ and $V_{pp\pi}(\mathbf{r}) = V_{pp\pi}^0 \exp\{q_\pi(1 - |\mathbf{r}|/a)\} \Theta(R_c - |\mathbf{r}|)$. It take the pre-factor for the $pp\sigma$ -hopping and $pp\pi$ -hopping to be $V_{pp\sigma}^0 = 0.48 \text{ eV}$ and $V_{pp\pi}^0 = -2.7 \text{ eV}$, respectively. The carbon-carbon bond length is given by $a = a_0/\sqrt{3}$ and the interlayer separation was taken to be $d_{AB} = 3.35 \text{ \AA}$. It take the decay parameters of the SK rules to be $q_\sigma = d_{AB}/0.184a_0$ and $q_\pi = 1/0.184\sqrt{3}$.^[36,37] Hoppings between carbon atoms separated by more than $R_c = 10 \text{ \AA}$ were neglected.^[130]

These atomistic methods, using the KC potential and SK rules,^[36,37] had been commonly employed within the community to study TBG.^[125,130,131] However, it was known that the KC potential had some shortcomings, with an example of a more accurate potential being developed by Wen et al.^[132] Moreover, the SK rules for the tight-binding parameters were simple, but were known to disagree with those obtained from wannierization of the electronic structure of graphene, with Pathak et al.^[133] developing a more accurate tight-binding model for TBG. While the atomistic methods here, also commonly employed by others, were not the most accurate for graphene-based moiré systems, it had been shown that these simplified methods could accurately reproduce the DFT electronic structure with only small changes to the tight-binding parameters.^[35,134] The main difference for the presented study and those of more accurate models was the exact twist angle of the magic angle, and therefore, the results presented were not very sensitive to the exact atomistic model used.

To include the effects of short-range Hubbard interactions, the on-site energy is determined by the mean-field Hubbard interaction^[77]

$$\epsilon_{i\sigma} = Un_{i\sigma'}, \quad (6)$$

where U is the Hubbard parameter of the carbon p_z orbital, and $n_{i\sigma'}$ is the mean-field electron density on atom i with the spin σ' being the opposite to σ .^[77] Note that in the mean-field Hubbard calculations it only consider collinear spin configurations.

The electron density could be determined from the Bloch eigenstates $\psi_{nk\sigma}(\mathbf{r})$ (with subscripts n and \mathbf{k} denoting a band index and the crystal momentum, respectively) according to

$$\begin{aligned} n_{\sigma}(\mathbf{r}) &= \sum_{nk} f_{nk\sigma} |\psi_{nk\sigma}(\mathbf{r})|^2 \\ &= \sum_j n_{j\sigma} \chi_j(\mathbf{r}) \end{aligned} \quad (7)$$

where $f_{nk\sigma} = \Theta(\epsilon_F - \epsilon_{nk\sigma})$ is the occupancy of state $\psi_{nk\sigma}$ with eigenvalue $\epsilon_{nk\sigma}$ (where ϵ_F is the Fermi energy), $\chi_j(\mathbf{r}) = \sum_{\mathbf{R}} \phi_z^2(\mathbf{r} - \mathbf{t}_j - \mathbf{R})$ (with \mathbf{R} denoting the moiré lattice vectors, $\phi_z(\mathbf{r})$ being the carbon p_z orbital and \mathbf{t}_j denoting the position vector of atom j relative to the origin of the moiré unit cell) and $n_{j\sigma}$ is the total number of electrons in the j -th orbital with spin σ .^[69] To characterize the magnetic ordering, it calculates the spin polarization

$$\zeta_j = \frac{n_{j\uparrow} - n_{j\downarrow}}{n_{j\uparrow} + n_{j\downarrow}} \quad (8)$$

To obtain a solution of the atomistic Hubbard model, it must perform self-consistent calculations in order to converge the electron density. To prepare the mean-field calculations in a magnetic state, it required an initial guess for the electron densities $n_{j\sigma}$. For this, it performed RPA spin-susceptibility calculations, following the methods outlined in Refs. [65, 66]. The eigenvalues of these calculations provide the critical interaction strength of a magnetic instability (U_c) and the eigenvectors describe the spatial profile of the magnetic order. By using these eigenvectors as an initial on-site interaction, as shown in Ref. [65], we induce a spin polarization of the same form. The resulting electron density of which could then be used to perform self-consistent calculations.

To obtain a self-consistent solution, it used a simple mixing scheme with a mixing parameter of 0.1 typically (0.1 of the new electron spin density was mixed into the spin density of the previous step). When determining the Fermi energy, the total electron number was again forced to be N , as it only study charge neutrality here, but this did not restrict the spin densities to be the same. It mixed the up and down spin density by the same amount, instead of choosing to work with the total electron density and magnetic order parameter, as it found it is sometimes more stable.

Using this approach, it was only possible to stabilize the leading instability obtained from the RPA calculations.^[83] To study the other magnetic orderings, it also perform constrained calculations. In these calculations,

it first determine an analytical form for the spatial profile of the magnetic order in terms of a few parameters and then optimize the value of these parameters, see Section 2.1.

Continuum Model Calculations: The mini-Brillouin Zone (mBZ) of the continuum model was spanned by the two reciprocal lattice vectors $\mathbf{G}_1 = \frac{2\pi}{L_m} (\frac{1}{\sqrt{3}}, 1)$ and $\mathbf{G}_2 = \frac{4\pi}{L_m} (-\frac{1}{\sqrt{3}}, 0)$, where $L_m = \frac{a_0}{2 \sin(\theta/2)}$ is the moiré period and a_0 is the lattice constant of graphene. These vectors form the basis to define any reciprocal lattice vector, $\mathbf{G}_i = n\mathbf{G}_1 + m\mathbf{G}_2$ with $n, m \in \mathbb{Z}$, $i \in \mathbb{N}$. The first star of reciprocal lattice vectors, i.e., the six first \mathbf{G}_i , are defined by $n, m \in [-1, 1]$.

The non-interacting continuum model was four-fold degenerate, since it accounts for valley and spin quantum numbers, with the Hamiltonian at crystal momentum \mathbf{k} being written as

$$\hat{H}_{TBC,\xi}(\mathbf{k}) = \begin{pmatrix} \hat{H}_{1,\xi}(\mathbf{k}) & \hat{\tau} \\ \hat{\tau}^\dagger & \hat{H}_{2,\xi}(\mathbf{k}) \end{pmatrix} \quad (9)$$

where $\hat{H}_{l,\xi}$ is the continuum single layer graphene Hamiltonian of valley ξ and layer l , given by

$$\hat{H}_{l,\xi}(\mathbf{k}) = \xi \hbar v_F (\mathbf{k} - \xi \mathbf{K}_l) \tau_{\theta,l} \quad (10)$$

with $v_F = (\sqrt{3}V_{pp}^0 a) / (2\hbar)$ denoting the Fermi velocity, \mathbf{K}_l is the position of the Dirac point of layer l , $\tau_{\theta,l} = e^{i\xi\tau_z\theta/2} (\tau_x, \xi\tau_y) e^{-i\xi\tau_z\theta/2}$, with τ_i being the Pauli matrices acting on the sublattice degree of freedom. The matrix $\hat{\tau}$ is a periodic function in the moiré unit cell that hybridizes layers. For small twist angles, the main contribution comes from the first three reciprocal lattice vectors, $\mathbf{G} = (0, 0)$, $\mathbf{G} = \mathbf{G}_1$ and $\mathbf{G} = \mathbf{G}_1 + \mathbf{G}_2$ ^[38]

$$\begin{aligned} \hat{\tau} = \sum_{\mathbf{G}} \hat{\tau}(\mathbf{G}) &= \begin{pmatrix} u_1 & u_2 \\ u_2 & u_1 \end{pmatrix} + \begin{pmatrix} u_1 & u_2 e^{-2i\theta\pi/3} \\ u_2 e^{2i\theta\pi/3} & u_1 \end{pmatrix} \\ &+ \begin{pmatrix} u_1 & u_2 e^{2i\theta\pi/3} \\ u_2 e^{-2i\theta\pi/3} & u_1 \end{pmatrix} \end{aligned} \quad (11)$$

where $u_1 = 0.0797$ eV and $u_2 = 0.0975$ eV^[135] are, respectively, the hopping amplitudes between AB/BA and AA stacking, which incorporate the atomic relaxation in the continuum model.^[124,135,136]

To account for electron-electron interactions, it include the mean-field Hartree-Fock terms to the Hamiltonian, assuming a collinear configuration of spins in which they were aligned either in a parallel or in an antiparallel manner along a specific direction. The Hartree contribution to the Hamiltonian is given by

$$\hat{H}_H = \sum_{i,\xi,\sigma} \int_{\Omega} d2\mathbf{r} \hat{\psi}_{\xi,\sigma}^{i,\dagger}(\mathbf{r}) \hat{\psi}_{\xi,\sigma}^i(\mathbf{r}) V_H(\mathbf{r}) \quad (12)$$

where $i \in [1, 4]$ labels the combined sublattice and layer degree of freedom, σ accounts for the spin, Ω is the area of the TBG sheet, and the local Hartree potential is given by

$$V_H(\mathbf{r}) = \int_{\Omega} d2\mathbf{r}' v_C(\mathbf{r} - \mathbf{r}') \langle \delta \hat{\rho}(\mathbf{r}') \rangle \quad (13)$$

here $\delta \hat{\rho}(\mathbf{r}) \equiv \hat{\rho}(\mathbf{r}) - \rho_{CN}(\mathbf{r})$ denotes the fluctuation in charge density, with $\hat{\rho}(\mathbf{r}) = \sum_{\xi,\sigma} \hat{\psi}_{\xi,\sigma}^\dagger(\mathbf{r}) \hat{\psi}_{\xi,\sigma}(\mathbf{r})$ corresponding to the charge density and $\rho_{CN}(\mathbf{r})$ is the average density of non-interacting TBG at charge neutrality. It assumed that the Coulomb interaction was screened by a double-metallic gate^[51]

$$v_C(\mathbf{q}) = \frac{2\pi e^2 \tanh(d|q|)}{\epsilon |q|} \quad (14)$$

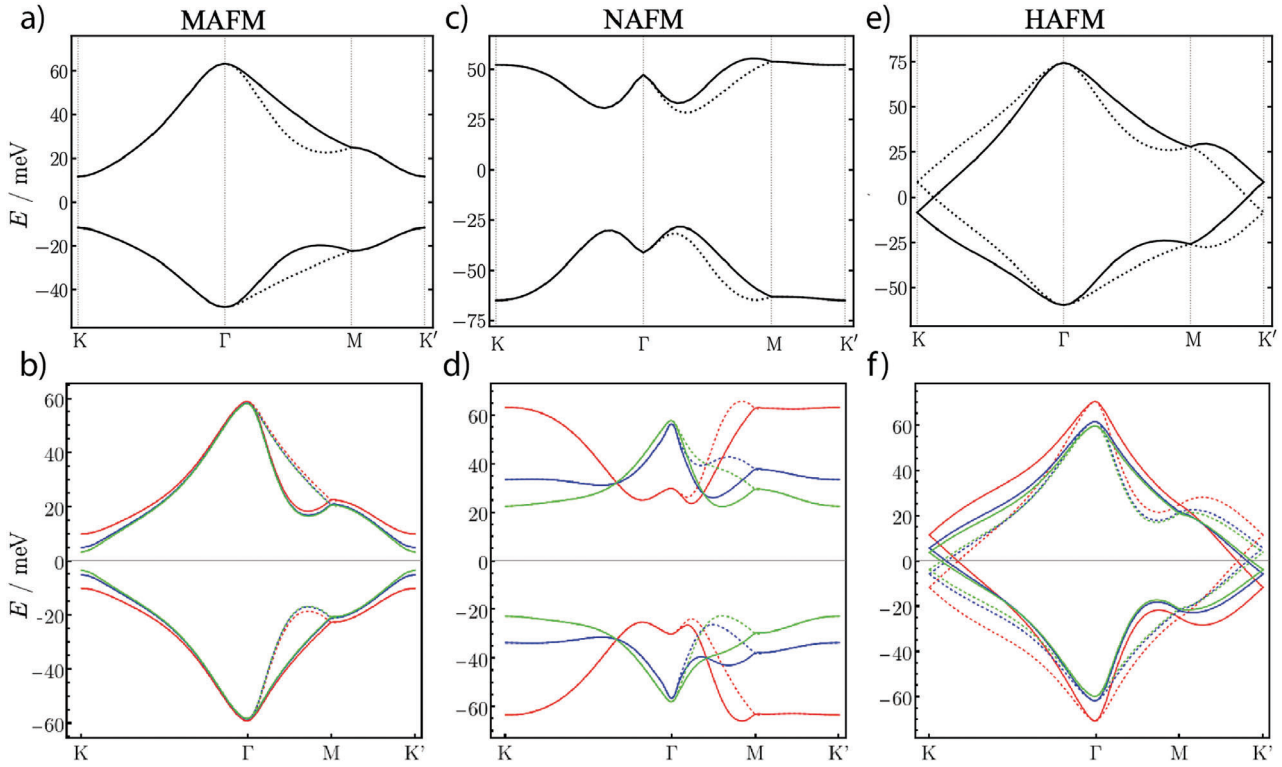


Figure A1. Low energy band structure for $\theta = 1.54^\circ$, along the path $K \rightarrow \Gamma \rightarrow M \rightarrow K'$ in the mBZ. a) With MAFM potential in the Tight-Binding approximation, b) with MAFM potential in the continuum approximation and scaling factor $f = 1$ (red), $f = 1/2$ (blue) and $f = 1/3$ (green). c) With NAFM potential in the Tight-Binding approximation, d) with NAFM potential in the continuum approximation and similar color-scheme than in (b). e) With HAFM potential in the Tight-Binding approximation, f) with HAFM potential in the continuum approximation and similar color-scheme than in (b). Dashed lines correspond to valley flip.

where $d = 40$ nm is the distance to the metallic gates and $\epsilon = 10$ is the background dielectric constant.^[42,60,69]

The Fock contribution to the Hamiltonian is given by

$$\hat{H}_F = \sum_{i,j,\xi,\sigma} \int_{\Omega} d2r d2r' \hat{\psi}_{\xi,\sigma}^{i,\dagger}(\mathbf{r}) V_F^{ij}(\mathbf{r}, \mathbf{r}') \hat{\psi}_{\xi,\sigma}^j(\mathbf{r}') \quad (15)$$

where i, j run over the sublattice and layer indexes. The non-local Fock potential is given by

$$V_F^{ij} = -\langle \hat{\psi}_{\xi,\sigma}^{i,\dagger}(\mathbf{r}') \hat{\psi}_{\xi,\sigma}^i(\mathbf{r}) \rangle v_C(\mathbf{r} - \mathbf{r}') \quad (16)$$

As it want to express the matrix elements of \hat{H}_F , defined in Equation (15), in reciprocal space it must transform the non-local Fock potential into Fourier space. By this procedure the field operators reduce to,

$$\hat{\psi}_{\xi,\sigma}^i(\mathbf{r}) = \frac{1}{\sqrt{\Omega}} \sum_{\mathbf{k}, \mathbf{G}} \phi_{\xi,\sigma}^i(\mathbf{k} + \mathbf{G}) e^{i(\mathbf{k} + \mathbf{G}) \cdot \mathbf{r}} \quad (17)$$

and the Fock matrix elements can be computed as

$$\begin{aligned} & \langle \mathbf{k} + \mathbf{G}, \xi, \sigma, i | \hat{H}_F | \mathbf{k}' + \mathbf{G}', \xi', \sigma', i' \rangle = \\ & -\frac{1}{\Omega} \sum_{i,j,\xi,\sigma} \sum_{\mathbf{k}'', \mathbf{G}''} \phi_{\xi,\sigma}^i(\mathbf{k} + \mathbf{G}' + \mathbf{G}'') \phi_{\xi,\sigma}^{j,*}(\mathbf{k}' + \mathbf{G} + \mathbf{G}'') \\ & \times v_C(\mathbf{k} - \mathbf{k}'' + \mathbf{G}'') \end{aligned} \quad (18)$$

where the sum was over the occupied states at a given Fermi energy and ϕ are the wavefunctions. For the Hartree-Fock calculations it work with a continuum model of TBG expanded up to the third star. It used a density of k-points between $2 - 6 \times 10^5 \text{ \AA}^2$ in the mBZ, depending on the twisting angle, which provides converged results. The convergence of the Hartree-Fock potential was normally reached after 5 – 6 self-consistency steps.

The additional potential associated with the different magnetic orderings was included in the continuum model via a scalar sublattice and spin dependent potential expressed through its harmonic decomposition in the first star reciprocal lattice vectors according to

$$\hat{H}_{\xi}^{\alpha}(\mathbf{G}_i, \mathbf{G}_j) = \sum_{i,j=0}^6 U_{\xi}^{\alpha}(\mathbf{G}_i - \mathbf{G}_j) \quad (19)$$

where α labels the different magnetic orderings. As discussed in the Results Section, this were able to express the potential from Hubbard interactions in the atomistic model through a Fourier series with only a constant and the first star of moiré \mathbf{G} vectors. A general expression for the potential in real space induced by these anti-ferromagnetic instabilities would be

$$\begin{aligned} U_{\xi}^{\alpha}(\mathbf{r}) = & \delta_1 \tau_z \\ & + \frac{1}{6} \sum_{i=1}^6 \delta_2 \tau_z \begin{cases} e^{i\mathbf{G}_i \cdot \mathbf{r}}, & \text{if } \alpha = \text{MAFM, NAFM} \\ e^{i\mathbf{G}_i \cdot \mathbf{r}}, & \text{if } \alpha = \text{HAFM.} \end{cases} \end{aligned} \quad (20)$$

where δ_1 corresponds to the average value of the sublattice polarization strength, δ_2 is the moiré modulated part of the potential, i.e., the weight associated to the expansion of the potential in the i -th BZ reciprocal lattice vector, and τ_z is the Pauli matrix corresponding to the sublattice degree

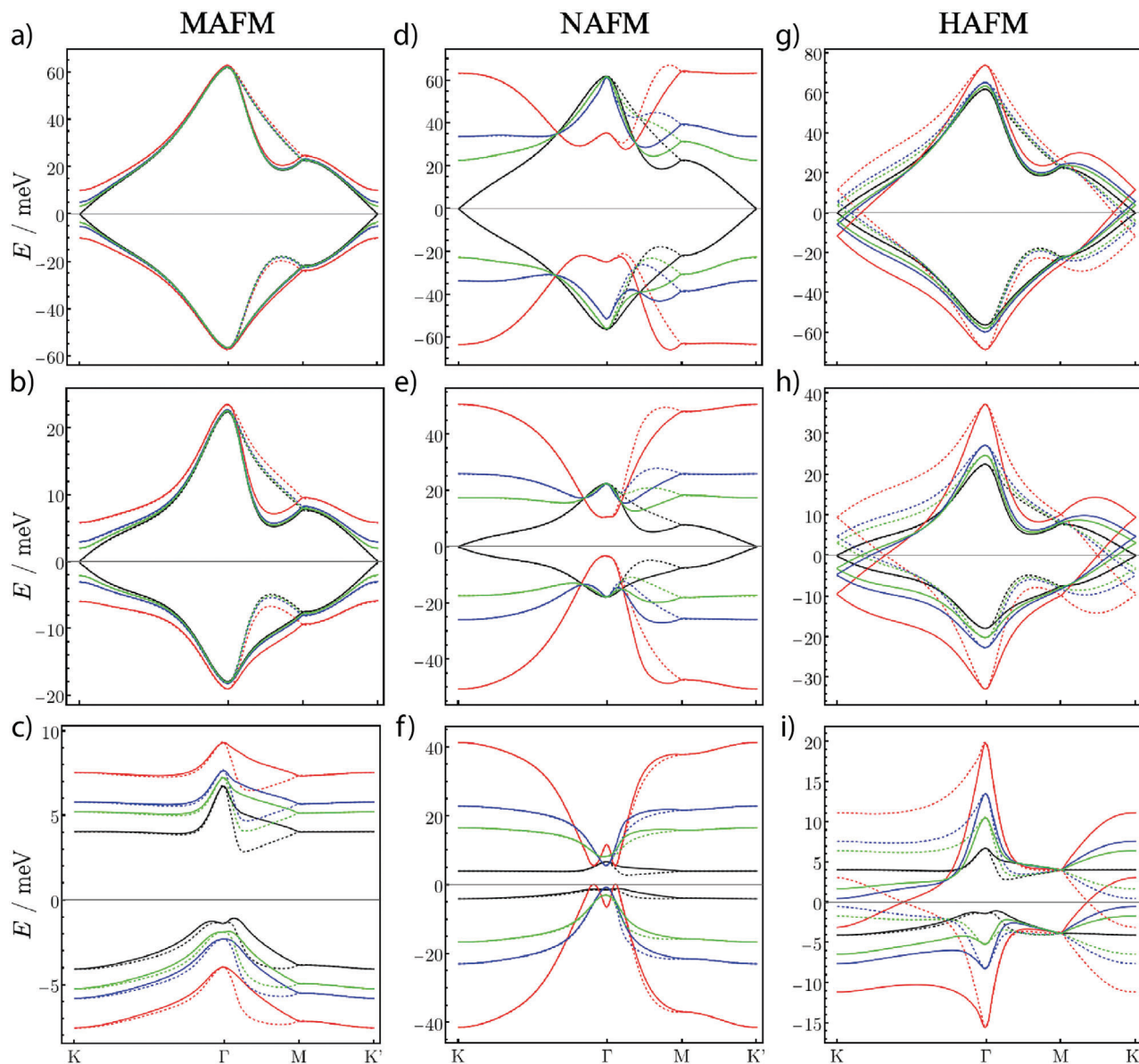


Figure A2. Low energy band structure along the path $K \rightarrow \Gamma \rightarrow M \rightarrow K'$ in the mBZ. a,b,c) with HF (black) and with MAFM+HF potentials in the continuum approximation and scaling factor $f=1$ (red), $f=1/2$ (blue) and $f=1/3$ (green). d,e,f) with HF (black) and with NAFM+HF potentials in the continuum approximation and scaling factor $f=1$ (red), $f=1/2$ (blue) and $f=1/3$ (green). g,h,i) with HF (black) and with HAFM+HF potentials in the continuum approximation and scaling factor $f=1$ (red), $f=1/2$ (blue) and $f=1/3$ (green). Dashed lines correspond to valley flip.

of freedom. The values for $\delta_{1/2}$ could be extracted from the atomistic calculations from the constant and first moiré \mathbf{G} vector variations in Un_σ , which were the main contributions. This real space potential was Fourier transformed and included in the Hamiltonian according to Equation (19).

The final Hamiltonian that combines both the effective magnetic potential derived from atomistic calculations and the Hartree-Fock potential is given by

$$\hat{H}_\xi(\mathbf{k}) = \hat{H}_{TBC,\xi}(\mathbf{k}) + \hat{H}_H(\mathbf{k}) + \hat{H}_F(\mathbf{k}) + \hat{H}_\xi^\alpha \quad (21)$$

It performed the calculation at half-filling and hence Hartree term was not included explicitly. Note that this final Hamiltonian was not treated in a self-consistent way since the effective magnetic Hamiltonian was just added to the self-consistent Hartree-Fock Hamiltonian, which would be equivalent to a first-order approximation of the magnetic orderings in per-

turbation theory. The band structures were obtained from diagonalizing this Hamiltonian.

Appendix: Scaling Factor

Following the explanation in Section 2.1 the RPA spin-susceptibility calculations of TBG at 1.54° show that the MAFM order is the leading instability in the system and requires a critical Hubbard interaction $U_c \approx 5.1$ eV to emerge. While the NAFM and HAFM orders necessitate a slightly higher interaction strength $U_c \approx 5.4$ eV. Initially, we performed atomistic Hubbard calculations with values of U larger than these critical values to readily stabilise the MAFM, NAFM, and HAFM magnetic orders. The converged self-consistent values of the electron density, and the value of U , was then used

to estimate the Hubbard potentials parameters of the continuum model at angles closer to the magic angle.

Given that the values of U used to converge the atomistic Hubbard calculations were larger than the physical value, $U \approx 4.5$ eV^[77,85,86] we must include into the continuum model a scaling factor f to obtain more physical results. Just based on the different values of U , from the physical value^[77,85,86] to those used to converge the atomistic calculations, one would at least need $f = 4.5/5.4 \approx 0.83$. The larger value of U also causes the spin density to be polarized more than it would be for the physical value, making the scaling factor depend non-trivially on the value of U . Therefore, as we do not know the exact scaling factor, we demonstrate that the results presented here are robust with respect to different values of the scaling factor.

In **Figure A1** we show the band structure of TBG at $\theta = 1.54^\circ$ with the magnetic potentials treated within the atomistic approach in the top row, and in the bottom row, we show the corresponding band structure within the continuum model (without the exchange potential contribution) for a scaling factor of $f = 1$ (red), $f = \frac{1}{2}$ (blue) $f = \frac{1}{3}$ (green). For the scaling factors considered it is clear that the band structures are qualitatively similar in the MAFM and HAFM cases; while in the NAFM case there appears to be significant differences, but this is because the gap at the K/K' point is larger than the bandwidth at this angle.

We perform a sanity check and show that once we include the exchange potential the differences vanish and the scaling factor does not play any role to derive the conclusions of the work. In **Figure A2a,d,g**, we plot the band structure of TBG for $\theta = 1.54^\circ$ with the magnetic and exchange potentials. In **Figure A2b,e,h** we plot again the band structure for $\theta = 1.25^\circ$ and in **Figure A2c,f,i** for $\theta = 1.05^\circ$. If we focus first on the $\theta = 1.54^\circ$ and $\theta = 1.25^\circ$ band structures in which the magnetic potentials dominates over the exchange potential, we notice that the role of the scaling factors $f = 1/2$ and $f = 1/3$ is just to decrease the magnitude of the gap near the K/K' points, leaving qualitatively the same band structure as for $f = 1$. While in the case of the magic angle $\theta = 1.05^\circ$ in which the exchange potential dominates, we note that in general for all the magnetic potentials taken into account the scaling factor is responsible of controlling the overall bandwidth since the gap is due to the exchange potential. In this sense, we note that the interplay between magnetic and exchange potentials is not affected by choosing any of the scaling factors considered in the work and so the conclusions derived from this interplay. We then choose the scaling factor to be $f = 1/3$ so the bandwidth is more reliable to the ones experimentally reported near the magic angle.

Acknowledgements

A.J.P., P.A.P., and F.G. acknowledge support from the Severo Ochoa programme for centres of excellence in R&D (Grant no. SEV-2016-0686, Ministerio de Ciencia e Innovación, Spain); from the European Commission, within the Graphene Flagship, Core 3, grant number 881603 and from grants NEMAT2D (Comunidad de Madrid, Spain) and SprQuMat (Ministerio de Ciencia e Innovación, Spain). ZG was supported through a studentship in the Centre for Doctoral Training on Theory and Simulation of Materials at Imperial College London funded by the EPSRC (EP/L015579/1). The authors acknowledge funding from EPSRC grant EP/S025324/1 and the Thomas Young Centre under grant number TYC-101. The authors acknowledge the Imperial College London Research Computing Service (DOI:10.14469/hpc/2232) for the computational resources used in carrying out this work. This project had received funding from the European Union's Horizon 2020 research and innovation programme under the Marie Skłodowska-Curie grant agreement no. 101067977. The Deutsche Forschungsgemeinschaft (DFG, German Research Foundation) was acknowledged for support through RTG 1995, within the Priority Program SPP 2244 "2DMP" - 443273985 and under Germany's Excellence Strategy-Cluster of Excellence Matter and Light for Quantum Computing (ML4Q) EXC2004/1 - 390534769. The authors acknowledge support from the Max Planck-New York City Center for Non-Equilibrium Quantum Phenomena. Spin susceptibility calculations were

performed with computing resources granted by the RWTH Aachen University under projects rwth0496 and rwth0589.

Conflict of Interest

The authors declare no conflict of interest.

Data Availability Statement

The data that support the findings of this study are available from the corresponding author upon reasonable request.

Keywords

graphene, magnetism, twisted bilayer graphene

Received: May 5, 2023

Revised: July 20, 2023

Published online: August 13, 2023

- [1] S. Carr, S. Fang, E. Kaxiras, *Nat. Rev. Mater.* **2020**, *5*, 748.
- [2] S. Carr, D. Massatt, S. Fang, P. Cazeaux, M. Luskin, E. Kaxiras, *Phys. Rev. B* **2017**, *95*, 075420.
- [3] D. M. Kennes, M. Claassen, L. Xian, A. Georges, A. J. Millis, J. Hone, C. R. Dean, D. N. Basov, A. Pasupathy, A. Rubio, *Nat. Phys.* **2021**, *17*, 155.
- [4] Y. Cao, V. Fatemi, A. Demir, S. Fang, S. L. Tomarken, J. Y. Luo, J. D. Sanchez-Yamagishi, K. Watanabe, T. Taniguchi, E. Kaxiras, R. C. Ashoori, P. Jarillo-Herrero, *Nature* **2018**, *556*, 80.
- [5] Y. Cao, V. Fatemi, S. Fang, K. Watanabe, T. Taniguchi, E. Kaxiras, P. Jarillo-Herrero, *Nature* **2018**, *556*, 43.
- [6] Y. Cao, J. Y. Luo, V. Fatemi, S. Fang, J. D. Sanchez-Yamagishi, K. Watanabe, T. Taniguchi, E. Kaxiras, P. Jarillo-Herrero, *Phys. Rev. Lett.* **2016**, *117*, 116804.
- [7] L. Balents, C. R. Dean, D. K. Efetov, A. F. Young, *Nat. Phys.* **2020**, *16*, 725.
- [8] E. Y. Andrei, A. H. MacDonald, *Nat. Mater.* **2020**, *19*, 1265.
- [9] Y. Saito, J. Ge, K. Watanabe, T. Taniguchi, A. F. Young, *Nat. Phys.* **2020**, *16*, 926.
- [10] P. Stepanov, I. Das, X. Lu, A. Fahimniya, K. Watanabe, T. Taniguchi, F. H. L. Koppens, J. Lischner, L. Levitov, D. K. Efetov, *Nature* **2020**, *583*, 375.
- [11] M. Oh, K. P. Nuckolls, D. Wong, R. L. Lee, X. Liu, K. Watanabe, T. Taniguchi, A. Yazdani, *Nature* **2021**, *600*, 240.
- [12] Y. Cao, D. Chowdhury, D. Rodan-Legrain, O. Rubies-Bigordà, K. Watanabe, T. Taniguchi, T. Senthil, P. Jarillo-Herrero, *Phys. Rev. Lett.* **2019**, *124*, 076801.
- [13] H. Polshyn, M. Yankowitz, S. Chen, Y. Zhang, K. Watanabe, T. Taniguchi, C. R. Dean, A. F. Young, *Nat. Phys.* **2019**, *15*, 1011.
- [14] Y. Cao, D. Rodan-Legrain, J. M. Park, F. N. Yuan, K. Watanabe, T. Taniguchi, R. M. Fernandes, L. Fu, P. Jarillo-Herrero, *Science* **2021**, *372*, 264.
- [15] A. Kerelsky, L. J. McGilly, D. M. Kennes, L. Xian, M. Yankowitz, S. Chen, K. Watanabe, T. Taniguchi, J. Hone, C. Dean, A. Rubio, A. N. Pasupathy, *Nature* **2019**, *572*, 95.
- [16] Y. Jiang, X. Lai, K. Watanabe, T. Taniguchi, K. Haule, J. Mao, E. Y. Andrei, *Nature* **2019**, *573*, 91.
- [17] Y. Choi, J. Kemmer, Y. Peng, A. Thomson, H. Arora, R. Polski, Y. Zhang, H. Ren, J. Alicea, G. Refael, F. von Oppen, K. Watanabe, T. Taniguchi, S. Nadj-Perge, *Nat. Phys.* **2019**, *15*, 1174.

- [18] U. Zondiner, A. Rozen, D. Rodan-Legrain, Y. Cao, R. Queiroz, T. Taniguchi, K. Watanabe, Y. Oreg, F. von Oppen, A. Stern, E. Berg, P. Jarillo-Herrero, S. Ilani, *Nature* **2020**, *582*, 203.
- [19] D. Wong, K. P. Nuckolls, M. Oh, B. Lian, Y. Xie, S. Jeon, K. Watanabe, T. Taniguchi, B. A. Bernevig, A. Yazdani, *Nature* **2020**, *582*, 198.
- [20] A. Rozen, J. M. Park, U. Zondiner, Y. Cao, D. Rodan-Legrain, T. Taniguchi, K. Watanabe, Y. Oreg, A. Stern, E. Berg, P. Jarillo-Herrero, S. Ilani, *Nature* **2021**, *592*, 214.
- [21] Y. Saito, F. Yang, J. Ge, X. Liu, T. Taniguchi, K. Watanabe, J. I. A. Li, E. Berg, A. F. Young, *Nature* **2021**, *592*, 220.
- [22] S. Wu, Z. Zhang, K. Watanabe, T. Taniguchi, E. Y. Andrei, *Nat. Mater.* **2020**, *21*, 488.
- [23] K. P. Nuckolls, M. Oh, D. Wong, B. Lian, K. Watanabe, T. Taniguchi, B. A. Bernevig, A. Yazdani, *Nature* **2020**, *588*, 610.
- [24] I. Das, X. Lu, J. Herzog-Arbeitman, Z.-D. Song, K. Watanabe, T. Taniguchi, B. A. Bernevig, D. K. Efetov, *Nat. Phys.* **2021**, *17*, 710.
- [25] Y. Xie, A. T. Pierce, J. M. Park, D. E. Parker, E. Khalaf, P. Ledwith, Y. Cao, S. H. Lee, S. Chen, P. R. Forrester, K. Watanabe, T. Taniguchi, A. Vishwanath, P. Jarillo-Herrero, A. Yacoby, *Nature* **2021**, *600*, 439.
- [26] Y. Choi, H. Kim, C. Lewandowski, Y. Peng, A. Thomson, R. Polski, Y. Zhang, K. Watanabe, T. Taniguchi, J. Alicea, S. Nadj-Perge, *Nat. Phys.* **2021**, *17*, 1375.
- [27] M. Yankowitz, S. Chen, H. Polshyn, Y. Zhang, K. Watanabe, T. Taniguchi, D. Graf, A. F. Young, C. R. Dean, *Science* **2019**, *363*, 1059.
- [28] Y. Xie, B. Lian, B. Jäck, X. Liu, C.-L. Chiu, K. Watanabe, T. Taniguchi, B. A. Bernevig, A. Yazdani, *Nature* **2019**, *572*, 101.
- [29] X. Lu, P. Stepanov, W. Yang, M. Xie, M. A. Aamir, I. Das, C. Urgell, K. Watanabe, T. Taniguchi, G. Zhang, A. Bachtold, A. H. MacDonald, D. K. Efetov, *Nature* **2019**, *574*, 653.
- [30] A. L. Sharpe, E. J. Fox, A. W. Barnard, J. Finney, K. Watanabe, T. Taniguchi, M. A. Kastner, D. Goldhaber-Gordon, *Science* **2019**, *365*, 605.
- [31] M. Serlin, C. L. Tschirhart, H. Polshyn, Y. Zhang, J. Zhu, K. Watanabe, T. Taniguchi, L. Balents, A. F. Young, *Science* **2020**, *367*, 900.
- [32] H. Yoo, R. Engelke, S. Carr, S. Fang, K. Zhang, P. Cazeaux, S. H. Sung, R. Hovden, A. W. Tsien, T. Taniguchi, K. Watanabe, G.-C. Yi, M. Kim, M. Luskin, E. B. Tadmor, E. Kaxiras, P. Kim, *Nat. Mater.* **2019**, *18*, 448.
- [33] A. Uri, S. Grover, Y. Cao, J. A. Crosse, K. Bagani, D. Rodan-Legrain, Y. Myasoedov, K. Watanabe, T. Taniguchi, P. Moon, M. Koshino, P. Jarillo-Herrero, E. Zeldov, *Nature* **2020**, *581*, 47.
- [34] K. Uchida, S. Furuya, J.-I. Iwata, A. Oshiyama, *Phys. Rev. B* **2014**, *90*, 155451.
- [35] P. Lucignano, D. Alfé, V. Cataudella, D. Ninno, G. Cantele, *Phys. Rev. B* **2019**, *99*, 195419.
- [36] G. T. de Laissardière, D. Mayou, L. Magaud, *Nano Lett.* **2010**, *10*, 804.
- [37] G. T. de Laissardière, D. Mayou, L. Magaud, *Phys. Rev. B* **2012**, *86*, 125413.
- [38] J. M. B. Lopes dos Santos, N. M. R. Peres, A. H. Castro Neto, *Phys. Rev. Lett.* **2007**, *99*, 256802.
- [39] J. M. B. Lopes dos Santos, N. M. R. Peres, A. H. Castro Neto, *Phys. Rev. B* **2012**, *86*, 155449.
- [40] R. Bistritzer, A. H. MacDonald, *PNAS* **2011**, *108*, 12233.
- [41] F. Guinea, N. R. Walet, *PNAS* **2018**, *115*, 13174.
- [42] T. Cea, F. Guinea, *Phys. Rev. B* **2020**, *102*, 045107.
- [43] T. Cea, F. Guinea, *PNAS* **2021**, *118*, e2107874118.
- [44] C. Lewandowski, S. Nadj-Perge, D. Chowdhury, *npj Quantum Mater.* **2021**, *6*, 82.
- [45] G. Wagner, Y. H. Kwan, N. Bultinck, S. H. Simon, S. Parameswaran, *Phys. Rev. Lett.* **2022**, *128*, 156401.
- [46] M. Xie A. H. MacDonald, *Phys. Rev. Lett.* **2020**, *124*, 097601.
- [47] N. Bultinck, E. Khalaf, S. Liu, S. Chatterjee, A. Vishwanath, M. P. Zaletel, *Phys. Rev. X* **2020**, *10*, 031034.
- [48] J. Liu, X. Dai, *Phys. Rev. B* **2021**, *103*, 035427.
- [49] Y. Zhang, K. Jiang, Z. Wang, F. Zhang, *Phys. Rev. B* **2020**, *102*, 035136.
- [50] T. Cea, P. A. Pantaleón, N. R. Walet, F. Guinea, *Nano Mater. Sci.* **2022**, *4*, 27.
- [51] T. Cea, N. R. Walet, F. Guinea, *Phys. Rev. B* **2019**, *100*, 205113.
- [52] L. Zou, H. C. Po, A. Vishwanath, T. Senthil, *Phys. Rev. B* **2018**, *98*, 085435.
- [53] H. C. Po, L. Zou, A. Vishwanath, T. Senthil, *Phys. Rev. X* **2018**, *8*, 031089.
- [54] J. Kang, O. Vafek, *Phys. Rev. Lett.* **2019**, *122*, 246401.
- [55] K. Seo, V. N. Kotov, B. Uchoa, *Phys. Rev. Lett.* **2019**, *122*, 246402.
- [56] M. Calderón, E. Bascones, *Phys. Rev. B* **2020**, *102*, 155149.
- [57] S. Carr, S. Fang, H. C. Po, A. Vishwanath, E. Kaxiras, *Phys. Rev. Res.* **2019**, *1*, 033072.
- [58] Z. A. H. Goodwin, F. Corsetti, A. A. Mostofi, J. Lischner, *Phys. Rev. B* **2019**, *100*, 121106(R).
- [59] Z. A. H. Goodwin, F. Corsetti, A. A. Mostofi, J. Lischner, *Phys. Rev. B* **2019**, *100*, 235424.
- [60] Z. A. H. Goodwin, V. Vitale, F. Corsetti, D. Efetov, A. A. Mostofi, J. Lischner, *Phys. Rev. B* **2020**, *101*, 165110.
- [61] D. M. Kennes, J. Lischner, C. Karrasch, *Phys. Rev. B* **2018**, *98*, 241407.
- [62] B. Roy, V. Juričić, *Phys. Rev. B* **2019**, *99*, 121407.
- [63] Y.-T. Hsu, F. Wu, S. Das Sarma, *Phys. Rev. B* **2020**, *102*, 085103.
- [64] E. Laksono, J. N. Leaw, A. Reaves, M. Singh, X. Wang, S. Adam, X. Gu, *Solid State Commun.* **2018**, *282*, 38.
- [65] L. Klebl, C. Honerkamp, *Phys. Rev. B* **2019**, *100*, 155145.
- [66] L. Klebl, Z. A. H. Goodwin, A. A. Mostofi, D. M. Kennes, J. Lischner, *Phys. Rev. B* **2021**, *103*, 195127.
- [67] A. Fischer, L. Klebl, C. Honerkamp, D. M. Kennes, *Phys. Rev. B* **2021**, *103*, L041103.
- [68] L. Rademaker, D. A. Abanin, P. Mellado, *Phys. Rev. B* **2019**, *100*, 205114.
- [69] Z. A. H. Goodwin, V. Vitale, X. Liang, A. A. Mostofi, J. Lischner, *Electron. Struct.* **2020**, *2*, 034001.
- [70] C. S. Cheung, Z. A. H. Goodwin, V. Vitale, J. Lischner, A. A. Mostofi, *Electron. Struct.* **2021**, *4*, 025001.
- [71] J. Vahedi, R. Peters, A. Missaoui, A. Honecker, G. T. de Laissardière, *SciPost Phys.* **2021**, *11*, 083.
- [72] J. González, T. Stauber, *Phys. Rev. B* **2021**, *104*, 115110.
- [73] J. González, T. Stauber, *Phys. Rev. B* **2020**, *102*, 081118.
- [74] A. O. Sboychakov, A. V. Rozhkov, A. L. Rakhmanov, F. Nori, *Phys. Rev. B* **2019**, *100*, 045111.
- [75] A. O. Sboychakov, A. V. Rozhkov, A. L. Rakhmanov, F. Nori, *Phys. Rev. B* **2020**, *102*, 155142.
- [76] D. V. Chichinadze, L. Classen, A. V. Chubukov, *Phys. Rev. B* **2020**, *101*, 224513.
- [77] L. A. Gonzalez-Arraga, J. L. Lado, F. Guinea, P. San-Jose, *Phys. Rev. Lett.* **2017**, *119*, 107201.
- [78] A. Ramires, J. L. Lado, *Phys. Rev. B* **2019**, *99*, 245118.
- [79] T. M. R. Wolf, J. L. Lado, G. Blatter, O. Zilberberg, *Phys. Rev. Lett.* **2019**, *123*, 096802.
- [80] S. Carr, S. Fang, P. Jarillo-Herrero, E. Kaxiras, *Phys. Rev. B* **2018**, *98*, 085144.
- [81] A. Lopez-Bezanilla, *Phys. Rev. Mater.* **2019**, *3*, 054003.
- [82] X. Chen, S. Liu, J. N. Fry, H.-P. Cheng, *J. Phys.: Condens. Matter.* **2022**, *34*, 385501.
- [83] Z. A. H. Goodwin, *PhD. Theory and simulation of moiré graphene multilayers*, Imperial College London, London **2022**.
- [84] A. Lopez-Bezanilla, J. L. Lado, *Phys. Rev. Res.* **2020**, *2*, 033357.
- [85] T. O. Wehling, E. Şaşıoğlu, C. Friedrich, A. I. Lichtenstein, M. I. Katsnelson, S. Blügel, *Phys. Rev. Lett.* **2011**, *106*, 236805.
- [86] M. Schüler, M. Rösner, T. O. Wehling, A. I. Lichtenstein, M. I. Katsnelson, *Phys. Rev. Lett.* **2013**, *111*, 036601.
- [87] T. Cea, N. R. Walet, F. Guinea, *Nano Lett.* **2019**, *19*, 8683.

- [88] P. A. Pantaleón, T. Cea, R. Brown, N. R. Walet, F. Guinea, *2D Mater.* **2021**, *8*, 044006.
- [89] P. J. Ledwith, E. Khalaf, Z. Zhu, S. Carr, E. Kaxiras, A. Vishwanath, arXiv:2111.11060 **2021**.
- [90] E. Khalaf, A. J. Kruchkov, G. Tarnopolsky, A. Vishwanath, *Phys. Rev. B* **2019**, *100*, 085109.
- [91] Z. Zhu, S. Carr, D. Massatt, M. Luskin, E. Kaxiras, *Phys. Rev. Lett.* **2020**, *125*, 116404.
- [92] S. Carr, C. Li, Z. Zhu, E. Kaxiras, S. Sachdev, A. Kruchkov, *Nano Lett.* **2020**, *20*, 3030.
- [93] A. Fischer, Z. H. Goodwin, A. A. Mostofi, J. Lischner, D. M. Kennes, L. Klebl, *npj Quantum Mater.* **2021**, *7*, 5.
- [94] V. T. Phong, P. A. Pantaleón, T. Cea, F. Guinea, *Phys. Rev. B* **2021**, *104*, L121116.
- [95] J. Shin, B. L. Chittari, J. Jung, *Phys. Rev. B* **2021**, *104*, 045413.
- [96] J. M. Park, Y. Cao, K. Watanabe, T. Taniguchi, P. Jarillo-Herrero, *Nature* **2021**, *590*, 249.
- [97] Y. Cao, J. M. Park, K. Watanabe, T. Taniguchi, P. Jarillo-Herrero, *Nature* **2021**, *595*, 526.
- [98] Z. Hao, A. M. Zimmerman, P. Ledwith, E. Khalaf, D. H. Najafabadi, K. Watanabe, T. Taniguchi, A. Vishwanath, P. Kim, *Science* **2021**, *371*, 1133.
- [99] S. Turkel, J. Swann, Z. Zhu, M. Christos, K. Watanabe, T. Taniguchi, S. Sachdev, M. S. Scheurer, E. Kaxiras, C. R. Dean, A. N. Pasupathy, *Science* **2022**, *376*, 193.
- [100] H. Kim, Y. Choi, C. Lewandowski, A. Thomson, Y. Zhang, R. Polski, K. Watanabe, T. Taniguchi, J. Alicea, S. Nadj-Perge, *Nature* **2022**, *606*, 494.
- [101] Y. Zhang, R. Polski, C. Lewandowski, A. Thomson, Y. Peng, Y. Choi, H. Kim, K. Watanabe, T. Taniguchi, J. Alicea, F. von Oppen, G. Refael, S. Nadj-Perge, *Science* **2022**, *377*, 1538.
- [102] G. W. Burg, E. Khalaf, Y. Wang, K. Watanabe, T. Taniguchi, E. Tutuc, *Nat. Mater.* **2022**, *21*, 884.
- [103] S. Xu, M. M. A. Ezzi, N. Balakrishnan, A. Garcia-Ruiz, B. Tsim, C. Mullan, J. Barrier, N. Xin, B. A. Piot, T. Taniguchi, K. Watanabe, A. Carvalho, A. Mishchenko, A. K. Geim, V. I. Fal'ko, S. Adam, A. H. C. Neto, K. S. Novoselov, Y. Shi, *Nat. Phys.* **2021**, *17*, 619.
- [104] S. Chen, M. He, Y.-H. Zhang, V. Hsieh, Z. Fei, K. Watanabe, T. Taniguchi, D. H. Cobden, X. Xu, C. R. Dean, M. Yankowitz, *Nat. Phys.* **2020**, *17*, 374.
- [105] Z. A. H. Goodwin, L. Klebl, V. Vitale, X. Liang, V. Gogtay, X. van Gorp, D. M. Kennes, A. A. Mostofi, J. Lischner, *Phys. Rev. Mater.* **2021**, *5*, 084008.
- [106] C. Shen, Y. Chu, Q. Wu, N. Li, S. Wang, Y. Zhao, J. Tang, J. Liu, J. Tian, K. Watanabe, T. Taniguchi, R. Yang, Z. Y. Meng, D. Shi, O. V. Yazyev, G. Zhang, *Nat. Phys.* **2020**, *16*, 520.
- [107] X. Liu, Z. Hao, E. Khalaf, J. Y. Lee, K. Watanabe, T. Taniguchi, A. Vishwanath, P. Kim, *Nature* **2020**, *583*, 221.
- [108] B. G. W, J. Zhu, T. Taniguchi, K. Watanabe, A. H. MacDonald, E. Tutuc, *Phys. Rev. Lett.* **2019**, *123*, 197702.
- [109] C. Zhang, T. Zhu, S. Kahn, S. Li, B. Yang, C. Herbig, X. Wu, H. Li, K. Watanabe, T. Taniguchi, S. Cabrini, A. Zettl, M. P. Zaletel, F. Wang, M. F. Crommie, *Nat. Commun.* **2021**, *12*, 2516.
- [110] C. Rubio-Verdú, S. Turkel, Y. Song, L. Klebl, R. Samajdar, M. S. Scheurer, J. W. F. Venderbos, K. Watanabe, T. Taniguchi, H. Ochoa, L. Xian, D. M. Kennes, R. M. Fernandes, Á. Rubio, A. N. Pasupathy, *Nat. Phys.* **2021**, *18*, 196.
- [111] Y. Cao, D. Rodan-Legrain, O. Rubies-Bigorda, J. M. Park, K. Watanabe, T. Taniguchi, P. Jarillo-Herrero, *Nature* **2020**, *583*, 215.
- [112] H. Zhou, T. Xie, T. Taniguchi, K. Watanabe, A. F. Young, *Nature* **2021**, *598*, 434.
- [113] H. Zhou, L. Holleis, Y. Saito, L. Cohen, W. Huynh, C. L. Patterson, F. Yang, T. Taniguchi, K. Watanabe, A. F. Young, *Science* **2022**, *375*, 774.
- [114] Y. Zhang, R. Polski, A. Thomson, É. Lantagne-Hurtubise, C. Lewandowski, H. Zhou, K. Watanabe, T. Taniguchi, J. Alicea, S. Nadj-Perge, *Nature* **2023**, *613*, 268.
- [115] P. A. Pantaleón, A. Jimeno-Pozo, H. Sainz-Cruz, V. T. Phong, T. Cea, F. Guinea, *Nat. Rev. Phys.* **2023**, *5*, 304.
- [116] A. Ghazaryan, T. Holder, M. Serbyn, E. Berg, *Phys. Rev. Lett.* **2021**, *127*, 247001.
- [117] A. Ghazaryan, T. Holder, E. Berg, M. Serbyn, *Phys. Rev. B* **2023**, *107*, 104502.
- [118] Z. Li, X. Kuang, A. Jimeno-Pozo, H. Sainz-Cruz, Z. Zhan, S. Yuan, F. Guinea, *Phys. Rev. B* **2023**, *108*, 045404.
- [119] T. Cea, P. A. Pantaleón, V. T. Phong, F. Guinea, *Phys. Rev. B* **2022**, *105*, 075432.
- [120] A. Jimeno-Pozo, H. Sainz-Cruz, T. Cea, P. A. Pantaleón, F. Guinea, *Phys. Rev. B* **2023**, *107*, L161106.
- [121] N. N. T. Nam, M. Koshino, *Phys. Rev. B* **2017**, *96*, 075311.
- [122] S. K. Jain, V. Juric'ić, G. T. Barkema, *2D Mater.* **2017**, *4*, 015018.
- [123] F. Gargiulo, O. V. Yazyev, *2D Mater.* **2018**, *5*, 015019.
- [124] F. Guinea, N. R. Walet, *Phys. Rev. B* **2019**, *99*, 205134.
- [125] X. Liang, Z. A. H. Goodwin, V. Vitale, F. Corsetti, A. Mostofi, J. Lischner, *Phys. Rev. B* **2020**, *102*, 155146.
- [126] S. Plimpton, *J. Comp. Phys.* **1995**, *117*, 1.
- [127] T. C. O'Connor, J. Andzelm, M. O. Robbins, *J. Chem. Phys.* **2015**, *142*, 024903.
- [128] A. N. Kolmogorov, V. H. Crespi, *Phys. Rev. B* **2005**, *71*, 235415.
- [129] J. C. Slater, G. F. Koster, *Phys. Rev.* **1954**, *94*, 1498.
- [130] M. Angeli, D. Mandelli, A. Valli, A. Amaricci, M. Capone, E. Tosatti, M. Fabrizio, *Phys. Rev. B* **2018**, *98*, 235137.
- [131] Y. W. Choi, H. J. Choi, *Phys. Rev. Lett.* **2021**, *127*, 167001.
- [132] M. Wen, S. Carr, S. Fang, E. Kaxiras, E. B. Tadmor, *Phys. Rev. B* **2018**, *98*, 235404.
- [133] S. Pathak, T. Rakib, R. Hou, A. Nevidomskyy, E. Ertekin, H. T. Johnson, L. K. Wagner, *Phys. Rev. B* **2022**, *105*, 115141.
- [134] G. Cantele, D. Alfè, F. Conte, V. Cataudella, D. Ninno, P. Lucignano, *Phys. Rev. Res.* **2020**, *2*, 043127.
- [135] M. Koshino, N. F. Q. Yuan, T. Koretsune, M. Ochi, K. Kuroki, L. Fu, *Phys. Rev. X* **2018**, *8*, 031087.
- [136] S. Carr, S. Fang, Z. Zhu, E. Kaxiras, *Phys. Rev. Res.* **2019**, *1*, 013001.